Coupling of the Radiative, Convective, and Surface Fluxes over the Equatorial Pacific

A. K. BETTS

West Pawlet, Vermont

W. RIDGWAY

Applied Research Corp., Landover, Maryland

(Manuscript received 20 January 1987, in final form 19 August 1987)

ABSTRACT

An idealized energy-balance model for a closed tropical circulation is first presented to illustrate the coupling between the net tropospheric radiative cooling, the surface fluxes and the mean subsidence away from the precipitation zones. Then a one-dimensional diagnostic model and a radiation model with boundary layer clouds are combined to explore this coupling for a specific region using mean sounding data over the tropical Pacific. The radiatively driven subsidence rate at the top of the convective boundary layer is approximately 35 mb day^{-1} (0.04 Pa s^{-1}) and is largely independent of boundary layer cloud fraction. The sensitivity of the corresponding convective heat flux profiles to the mass divergence profile and cloud fraction within the boundary layer is explored. Reasonable assumptions give realistic surface sensible and latent heat fluxes for this region of approximately 10 and 130 W m^{-2}. The paper illustrates the important background climatic control of the radiation field on the tropical surface fluxes.

1. Introduction

In the last decade, global monitoring systems have improved, and global numerical models have shifted from short to medium-range prediction and the simulation of climate. Experiments such as the First GARP (Global Atmospheric Research Program) Global Experiment (FGGE) have addressed the collection of a global dataset for numerical studies; the Tropical Oceans and Global Atmospheric project (TOGA) is exploring the coupling of the oceanic and atmospheric circulations; and the International Satellite Cloud Climatology Project (ISCCP) is developing a global climatology of atmospheric cloud fields and their role in the earth's radiation budget. In global modeling studies improvements in the radiative, convective and boundary layer parameterizations have had major impacts on the model climate after a few days' simulated time (Heckley, 1985, 1986; Albrecht et al., 1986).

This paper has two distinct parts. In section 2 we shall discuss the energy budget of an idealized circulation model for the tropics to illustrate the relationships between the tropospheric net radiative cooling, the surface fluxes and the mean subsidence in the descending branch of the circulation. In sections 3 to 6, we combine a one-dimensional diagnostic model and a radiation model with boundary layer clouds to explore the coupling of the radiation field, the subsidence, and the boundary layer and surface fluxes for a specific region using mean sounding data over the tropical Pacific.

We shall define the convective boundary layer (CBL) as the layer which is coupled to the surface heat and moisture fluxes. This includes the subcloud, cloud and inversion layers. Betts and Albrecht (1987) found that over the equatorial Pacific the top of the CBL is typically around 800 mb and is marked by a local maximum of saturation equivalent potential temperature (θ_{es}) and a minimum of equivalent potential temperature, θ_e. They also found that the CBL from the surface to the θ_{es} maximum had a characteristic mixing-line thermodynamic structure (Betts, 1982a,b), indicative of convective mixing between the surface and the CBL top.

We shall show that the surface latent heat flux, which is strongly coupled to the mean CBL subsidence, is also coupled to the radiative cooling rate. In one sense this is well known. On a global scale the release of latent heat from the condensation of the surface evaporation flux plays a major part in balancing the atmospheric radiative cooling (Riehl and Malkus, 1958; Riehl and Simpson, 1969). Yet in boundary layer and global modeling studies, the nature of this connection has not been fully explored. For example, mixed-layer models of the CBL have been used to study the response of model fluxes and CBL depth to varying the subsidence rate and the radiative cooling rate of the boundary layer (e.g., Lilly, 1968; Schubert, 1976; Albrecht et

Corresponding author address: Dr. Alan K. Betts, R.F.D. 1, West Pawlet, VT 05775.

al., 1979), but the intimate coupling on long time scales between the subsidence and atmospheric radiative cooling rates has been largely ignored in CBL modeling. In contrast, Charney (1975) has discussed the coupling of the radiative cooling and subsidence in maintaining the climate of the Sahara Desert. McBride and Gray (1980) have also shown there is strong coupling between the diurnal cycle and the vertical mass transport in convective regions. Sarachik (1978) has used a theoretical model to discuss the coupling of the radiative and convective fluxes in the determination of the ocean surface temperature and atmospheric structure on long time scales.

There are many possible perspectives on the controls on, for example, the surface latent heat flux. A traditional method of estimating locally the surface latent heat flux over the oceans on short time scales is to use the surface wind speed, surface drag coefficient and the difference in mixing ratio between the sea surface and mixed layer. Budget studies (Holland and Rasmusson, 1973; Augstein et al., 1973) have shown that the subsidence in the CBL plays a dominant role in controlling the surface latent heat flux on time scales of a few days. In this paper we shall focus primarily on the control of the surface latent heat flux through the coupling of the subsidence and the radiation fields.

2. Idealized energy balance of the tropical circulation

It is well known that in the tropical circulation there is an approximate balance of the radiative cooling and the latent heat release from condensation heating (Riehl et al., 1951; Riehl and Malkus, 1958; Riehl and Simpson, 1979). Although the export of heat by the atmosphere to midlatitudes is important to the general circulation, it is considerably smaller than the precipitation heating in the tropics (e.g., Lorenz, 1967; Oort and Rasmusson, 1971). Several authors have considered the energetic balance of the tropical circulation (e.g., Gray, 1973; Sarachik, 1978). We first present an idealized one-dimensional closed model for the tropical circulation (based on Sarachik, 1978), which shows how the subsidence outside the precipitation zones and the corresponding surface fluxes are coupled to the radiation field. We shall assume a steady state over a uniform ocean surface, and neglect horizontal advection and exports to midlatitudes. Conceptually this model includes the subsidence in the equatorial trough as well as the Hadley circulation and could be regarded as a zero-order thermodynamic model for the long-term energy balance of the tropics. Our purpose in discussing such an idealized model is to illustrate that on long time scales (several days) and large space scales (10^3–10^4 km), there is a background subsidence field in the tropics (away from the regions of deep precipitating convection, which occupy a small fractional area) which couples the surface fluxes to the radiation field. These balances are of great importance to the climate of a global model, on time scales of 5–10 days. Unlike Sarachik (1978), we shall assume here a fixed ocean-surface temperature, and the atmospheric radiative flux divergence will be given a representative value. We shall also introduce a mixed-layer model, following Betts (1983).

a. Single-cell tropical model

Figure 1a shows an idealized circulation in which a well-mixed CBL, with thermodynamic properties **M** [see Betts (1983, 1985) for this vector notation], flows into the ITCZ and ascends to exit (with thermodynamic properties $\mathbf{T}_2$) near the tropopause. Figure 1b shows schematically the corresponding saturation point or conserved variable diagram for this circulation. The air ascends from the CBL to near the tropopause, conserving approximately its equivalent potential temperature, θ_e, or moist static energy, $h = c_pT + gz + Lq$. Its water vapor is precipitated, and its potential temperature, θ, correspondingly increases. The outflow then descends with radiative cooling, conserving its (small) water vapor content to reenter the CBL with a lower θ and θ_e (point $\mathbf{T}_1$). It is then converted back to air with mixed-layer properties by ocean surface fluxes (equivalent to mixing with air with properties **O**), and the radiative flux divergence in the CBL. For this simple model, we assume the upper-level outflow is confined to a shallow layer and the subsidence, ω, is then independent of height between the CBL top and the outflow.

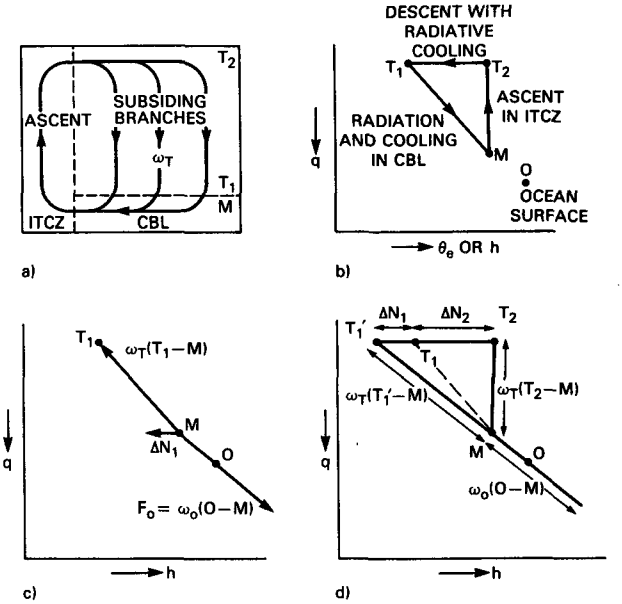

FIG. 1. Schematic for the idealized tropical circulation (Fig. 1a) with ascent in the ITCZ and uniform descent above a well-mixed CBL. (b) shows a conserved variable diagram for air making the circuit, (c) the thermodynamic vector balance for the mixed subcloud layer, and (d) the vector budget for the whole troposphere (see section 2d).

Consider the thermodynamic budget for the subsiding region. For the CBL, if we assume no horizontal advection and a steady state, we may write the one-dimensional vector thermodynamic budget (following Betts, 1983) as

$$\omega\partial\mathbf{S}/\partial p + g\partial\mathbf{N}/\partial p - g\partial\mathbf{F}/\partial p = 0. \quad (1)$$

The first term is the vertical advection of saturation point, S; the second relates to the net radiative flux divergence [proportional to the radiative cooling (heating) rate]; and the third to the divergence of the convective flux, which we have defined as positive upwards for convenience. If we integrate through the CBL and set the convective fluxes $\mathbf{F} = 0$ above the CBL, we get (Betts, 1983)

$$\omega_T(\mathbf{T}_1 - \mathbf{M}) - g\Delta\mathbf{N}_1 + g\mathbf{F}_0 = 0. \quad (2)$$

The first term represents the incorporation of (dry, low θ_e) air into the top of the CBL, the second the net radiative flux divergence within the CBL ($\Delta\mathbf{N}_1$ has been defined positive), and the third the surface heat and moisture fluxes. Figure 1c, which is discussed more in section 2f, summarizes the vector balance of these three terms.

Above the CBL in the subsiding branch (Fig. 1a)

$$\omega_T(\mathbf{T}_2 - \mathbf{T}_1) - g\Delta\mathbf{N}_2 = 0 \quad (3)$$

if we assume no convective fluxes or source terms above the CBL. Adding (2) and (3) we get for the whole subsiding branch (see Riehl et al., 1951)

$$\omega_T(\mathbf{T}_2 - \mathbf{M}) - g\Delta\mathbf{N} + g\mathbf{F}_0 = 0 \quad (4)$$

where

$$\Delta\mathbf{N} = \Delta\mathbf{N}_1 + \Delta\mathbf{N}_2$$

represents the net radiative cooling for the whole troposphere. Figure 1d summarizes this budget. Projecting (4) onto the q and θ_e axes gives

$$\omega_T(T_2 - M)_q + gF_q = 0 \quad (4a)$$

$$\omega_T(T_2 - M)_{\theta e} - g\Delta N_{\theta e} + gF_{\theta e} = 0. \quad (4b)$$

Equation (4a) summarizes the q budget of the troposphere and (4b) the θ_e budget. Because using static energies for atmospheric budgets has some advantages (Betts, 1974) (we are not considering the kinetic energy generation in this circulation), we shall use an equivalent form of (4b) incorporating the moist static energy (see Appendix):

$$\omega_T(T_2 - M)_h - g\Delta N + gF_h = 0 \quad (4c)$$

where ΔN is now simply the net tropospheric radiative flux difference. If we assume that h is approximately conserved in the ascending branch we can set

$$(T_2 - M)_h = (h_{T_2} - h_M) = 0 \quad (5)$$

and obtain

$$F_h - \Delta N = 0. \quad (6)$$

The two integral budgets [(4a) and (6)] are particularly illuminating for the tropical atmosphere on time scales of a week or so. As integral budgets for the tropics both are well known (Gray, 1973; Sarachik 1978), (4a) couples the surface evaporation to the ascending mass flux in the ITCZ and the compensating subsidence in the descending branch. Equation (6) couples the surface fluxes to the integrated radiative cooling, because for the tropics as a whole the surface latent heat flux is all precipitated (we have assumed no export of water vapor from the tropics).

We have shown, however, that these constraints (4a, 6) can be applied just to the subsiding branch of the tropical circulation, not simply to the whole tropical region. This is because the regions of ascent and precipitation in the tropics are small compared with the subsiding regions, so that any imbalance in ΔN and F_h in the precipitating regions [which we have neglected by using (5)], has little impact on (6) when averaged over the much larger subsiding domain.

Thus the Eqs. (4a) and (6) impose an important background constraint on the mean tropical circulation by coupling the surface and CBL fluxes to the radiation field through the tropospheric subsidence. This internally couples the tropospheric thermodynamic structure (Sarachik, 1978).

b. Mixed CBL model

We will now apply these constraints to a simple boundary layer model. Following Betts (1983), we parameterize the surface fluxes, using a surface velocity scale, ω_0, related to drag coefficient times wind speed:

$$g\mathbf{F}_0 = \omega_0(\mathbf{O} - \mathbf{M}). \quad (7)$$

Combining (7) and (2) gives

$$\omega_T(\mathbf{T}_1 - \mathbf{M}) - g\Delta\mathbf{N}_1 + \omega_0(\mathbf{O} - \mathbf{M}) = 0. \quad (8)$$

The q component of (8) does not contain the term in ΔN_1, and after rearrangement it gives the mixed-layer mixing ratio as a weighted average:

$$q_M = (\omega_T q_{T_1} + \omega_0 q_0)/(\omega_T + \omega_0). \quad (9)$$

We can use (9) to reexpress the surface latent heat flux from (7) in terms of a difference between ocean and atmosphere above the CBL (Betts, 1983)

$$F_{Lq} = L(q_0 - q_{T_1})\omega_0\omega_T/(\omega_0 + \omega_T)$$

$$= L(q_0 - q_{T_2})\omega_0\omega_T/(\omega_0 + \omega_T) \quad (10)$$

since $q_{T_1} = q_{T_2}$ (q is conserved in the descending branch).

Equation (6) contains the surface sensible heat flux (F_s) which is much smaller than F_{Lq}. We could neglect $F_s \ll F_{Lq}$, or use a mixed-layer model with entrainment closure to couple the CBL equations, but for simplicity we will assume a Bowen ratio, b (typically $b \approx 0.1$ over the oceans), so that

$$F_h = (1 + b)F_{Lq}. \quad (11)$$

Combining (11), (10), and (6) gives

$$L(q_0 - q_{T_2})\omega_0\omega_T/(\omega_0 + \omega_T) = gF_{Lq} = g\Delta N/(1 + b). \quad (12)$$

With rearrangement this important relationship gives

$$\omega_T = \omega_0/[\omega_0(1 + b)L(q_0 - q_{T_2})/g\Delta N - 1] \quad (13)$$

which links the subsidence to the surface wind speed (through ω_0), surface temperature (through q_0) and the radiative flux divergence for the troposphere. Equation (13) can be rewritten as

$$\omega_T = \omega_N/(1 - \omega_N/\omega_0) \quad (14)$$

by defining a velocity scale

$$\omega_N = g\Delta N/(1 + b)L(q_0 - q_{T_2}). \quad (15)$$

Since (14) can be rearranged as

$$\omega_N = \omega_0\omega_T/(\omega_0 + \omega_N),$$

these manipulations amount to writing (12) in the form

$$gF_{Lq} = L\omega_0(q_0 - q_M) = L\omega_N(q_0 - q_{T_2}). \quad (12a)$$

Thus ω_N is a bulk CBL transfer scale.

c. Approximations

If we neglect $q_{T_2} \ll q_0$, then from (12a)

$$(q_0 - q_M) \approx (\omega_N/\omega_0)q_0$$

$$q_M \approx (1 - \omega_N/\omega_0)q_0. \quad (16)$$

If we neglect $b \ll 1$

$$\omega_N \approx g\Delta N/Lq_0. \quad (15a)$$

Both (14) and (16) require $\omega_N/\omega_0 < 1$ for physically realistic solutions for q_M and the subsidence ω_T.

d. Typical magnitudes

Typical magnitudes over the tropical oceans are $q_0 \approx 22$ g kg^{-1}, corresponding to a surface temperature and pressure of 26.5°C and 1013 mb, and $\Delta N \approx 175$ W m^{-2} (estimated using the radiative model discussed in section 5). These give $\omega_N \approx 27$ mb day^{-1} (0.031 Pa s^{-1}) from (15a). A typical value for the surface velocity scale is $\omega_0 \approx 100$ mb day^{-1} (0.116 Pa s^{-1}). This corresponds to a surface wind speed of 7.8 m s^{-1} and surface drag coefficient of 1.3 10^{-3}. We see that $\omega_N/\omega_0 < 1$ as required in (14) and (16). Equation (14) then gives $\omega_T \approx 37$ mb day^{-1} (0.043 Pa s^{-1}).

So we see that the background radiatively driven subsidence is $\omega_T \approx 37$ mb day^{-1}, about a third of ω_0. From (16), $(q_0 - q_M) = (\omega_N/\omega_0)q_0 \approx 6$ g kg^{-1} so that the mean sea–air difference of mixing ratio and hence the mean height of cloud base (for small air–sea temperature differences) is linked to the net tropospheric radiative divergence. These values give a mixed-layer saturation pressure (a good estimate of cloud base) 72 mb above the surface for $b = 0$ and $\theta_0 = \theta_M$.

The surface fluxes for $b = 0.1$ are $F_s \approx 16$ W m^{-2} and $F_{Lq} \approx 159$ W m^{-2}, and the corresponding sea–air differences for $\omega_0 = 100$ mb day^{-1} (again neglecting q_{T_2}) are $(\theta_0 - \theta_M) \approx 1.3$ K and $(q_0 - q_M) \approx 5.4$ g kg^{-1}. These give a mixed-layer saturation level of 46 mb above the surface. Over the oceans the depth of the subcloud layer is typically in the range 40–70 mb (away from the convective disturbances). Equation (16) shows that this follows from the link between the surface fluxes and the troposphere radiative divergence, given typical surface wind speeds and Bowen ratios. For $b = 0.1$, the corresponding values of ω_N and ω_T from (15) and (14) are 24 and 32 mb day^{-1}, so that the radiatively driven subsidence is slightly reduced by including the contribution of the surface sensible heat flux to the heating of the atmosphere.

Equation (5) connects the moist static energy of the mixed layer and the top of the tropical deep convective layer: $h_M = h_{T_2} \approx s_{T_2}$, if we neglect q_{T_2}. From (6) and (7), we have h_M (which is independent of b):

$$h_0 - h_M = \omega_0\Delta N/g$$

so that $s_{T_2} = h_M = s_0 + Lq_0 = 341.3\ 10^3$ J kg^{-1}, for a surface temperature and pressure of 26.5°C and 1013 mb (which give $q_0 = 22$ g kg^{-1}).

If the stratospheric temperature is known (say −80°C), this gives 15 km as the height of the deep convective outflow, and the approximate height of the tropical tropopause. This also fixes the mean gradient of static energy or potential temperature in the troposphere at 2.75 10^3 J kg^{-1} km^{-1} (Sarachik, 1978), which is of course close to the mean gradient of the moist adiabat through cloudbase.

e. Limits

The limits on ω_N/ω_0 are of interest climatologically. We have seen that for present climate values $\omega_N/\omega_0 < 1$. With decreasing ω_N/ω_0 then, from (14) and (16), $\omega_T \to \omega_N$ and $q_M \to q_0$, so that the sea–air mixing ratio difference decreases with increasing mean tropical wind speeds. Conversely, as $\omega_N/\omega_0 \to 1$, (14) has a singularity and in (16) $q_M \to 0$. This corresponds to a very low mean surface wind speed of ≈ 2 m s^{-1}, when the surface latent heat flux can no longer balance ΔN. Clearly before this limit, our simple model with $b \ll 1$ must also fail, because once the tropospheric latent heat release is insufficient to balance ΔN (which in general must be computed), the air–sea temperature difference will increase.

f. Graphical solutions

Figure 1c summarizes the vector balance of the three terms in (2) after substituting (7), following Betts (1983) who showed how saturation point diagrams could summarize the CBL budgets. A more complete description of the budget for the whole tropical troposphere is given in Fig. 1d. Both figures use ω_T as a

scaling velocity. Figure 1d, following Betts (1983), defines a modified SP, $\mathbf{T}_1'$, using

$$\omega_T(\mathbf{T}_1' - \mathbf{T}_1) + g\Delta\mathbf{N}_1 = 0. \quad (17)$$

Using (3), (17) and (7) in (4) gives the mean tropical budget as the sum of three terms, representing the vertical advection, radiative cooling and surface fluxes

$$\omega_T(\mathbf{T}_2 - \mathbf{M}) + \omega_T(\mathbf{T}_1' - \mathbf{T}_2) + \omega_0(\mathbf{O} - \mathbf{M}) = 0. \quad (18)$$

This simplifies to just two balancing terms:

$$\omega_T(\mathbf{T}_1' - \mathbf{M}) + \omega_0(\mathbf{O} - \mathbf{M}) = 0, \quad (19)$$

showing that the mixed layer SP, **M**, is a weighted average of the SP's **O** and $\mathbf{T}_1'$, and hence $\mathbf{OMT}_1'$ is a mixing line (loc. cit.). Figure 1d summarizes (3), (17), (18) and (19) graphically. If we neglect the surface sensible heat flux, corresponding to $b = 0$ in (7) and (13), then the mixing line $\mathbf{OMT}_1'$ becomes a dry adiabat: i.e.,

$$\theta_0 = \theta_M = \theta_{T_1'},$$

or in static energy coordinates

$$s_0 = s_M = s_{T_1'}.$$

Our solution of (13) for $b = 0$ now corresponds to finding the q_M, ω_T, and s_{T_2} (given ΔN, ω_0, s_0, q_0, q_{T_2}) which simultaneously satisfy the three relationships:

$$\omega_0(q_0 - q_M) = \omega_T(q_M - q_{T_2}) \quad (20a)$$

$$\omega_T(s_{T_2} - s_0) = g\Delta N \quad (20b)$$

$$(s_{T_2} - s_0) = L(q_M - q_{T_2}) \quad (20c)$$

corresponding to the CBL moisture budget, the subsidence–radiation balance for the entire troposphere and the conservation of moist static energy between the CBL and upper troposphere.

For more complex boundary layer models these relationships can be extended and solved iteratively. The equilibrium depth of the CBL is not given by our analysis here, in which we have simply chosen a reasonable value of $\Delta\mathbf{N}$. This equilibrium depth is controlled by the requirements for consistency between $\Delta\mathbf{N}_1$ and $\Delta\mathbf{N}_2$ and the internal thermodynamic structure of the trophosphere [$\Delta\mathbf{N}_1$, $\Delta\mathbf{N}_2$ and $\mathbf{T}_1$ must satisfy (3) and (17)], as well as a more general closure condition for the CBL. These aspects we shall address in a later paper.

This conceptual model is useful in understanding the mean thermodynamic structure and surface fluxes of the tropics, and it gives an estimate of the magnitude of the mean tropospheric subsidence, but it contains idealizations which prohibit direct comparison with observations. We have assumed conservation of q and a constant value of ω_T above a well-mixed CBL, and assumed a value of $\Delta\mathbf{N}$. In the next section we shall present a diagnostic analysis of some mean tropical data from Betts and Albrecht (1987), where these assumptions are not satisfied, and show that similar estimates of the mean subsidence and the surface fluxes can be obtained, although the details of the CBL convective fluxes depend on the cloud fraction and mass divergence profile within the CBL. We shall use atmospheric data from the First GARP Global Experiment (FGGE) for the equatorial trough region of the Pacific during January and February 1979.

3. Diagnostic model for the CBL

We shall use a very simple, one-dimensional diagnostic model to explore the coupling of cloud fraction, subsidence, and the convective and radiative fluxes using mean atmospheric soundings. We start with the conservation equation (1) and integrate down from the top of the CBL to give the convective flux at level p:

$$\mathbf{F}(p) = g^{-1}\int_{p_{T_1}}^{p}(\omega\partial\mathbf{S}/\partial p)dp + [\Delta\mathbf{N}]_{p_{T_1}}^{p}. \quad (21)$$

As component equations we shall use the liquid water static energy ($s_l = c_pT + gz - Ll$) budget, derived from the liquid water potential temperature (θ_l) profile (see Appendix), and the Lq_t budget, where q_t is total water. Integrating down to the surface gives the surface fluxes of sensible heat

$$F_{0s} = g^{-1}\int_{p_{T_1}}^{p}\omega(T/\theta_l)(\partial\theta_l/\partial p)dp + \Delta N_1 \quad (22a)$$

and latent heat

$$F_{0Lq} = g^{-1}\int_{p_{T_1}}^{p}L\omega(\partial q_t/\partial p)dp. \quad (22b)$$

Equation (22b) does not contain the radiative flux divergence.

Within the CBL the radiative flux divergence can be computed from the cloud and thermodynamic distributions. We shall estimate the subsidence, ω_T, at the top of the CBL by using the θ component of (1) (with $F = 0$) averaged through a 50 mb layer just above the CBL:

$$\omega_T = [(g\overline{\partial N/\partial p})/c_p(\overline{T/\theta)(\partial\theta/\partial p)}] = \bar{\dot{\theta}}_N/(\overline{\partial\theta/\partial p}) \quad (23)$$

where the overbar denotes this 50 mb average, and $\dot{\theta}_N$ is the radiative cooling rate. This is the classic thermodynamic method for estimating the radiatively driven subsidence.

Given ω_T, the convective fluxes are still sensitive to the vertical distribution of divergence within the CBL. The simplest assumption would be to assume divergence constant with height, but tradewind budget studies (Holland and Rasmusson, 1973; Augstein et al., 1973) suggest that a quadratic profile for ω within the CBL may be a better approximation. Riehl et al. (1951) show a more complex structure for the divergence. We shall explore the sensitivity to different divergence profiles (see section 6).

In summary, in this diagnostic model the convective fluxes within the CBL are calculated from the subsidence and radiation fields, and the subsidence just above the CBL is estimated from radiative–subsidence balance. Within the CBL the radiation field and hence the derived convective fluxes are quite sensitive to cloud fraction and cloud-top distribution (see section 6), but the cooling rate and hence ω_T above the CBL are much less sensitive to the cloud parameters. The purpose of this simple model is to show that with a few assumptions on the internal CBL structure (the most important are the distribution of divergence and to a lesser extent the cloud fraction), we can get reasonable estimates of the surface fluxes of heat and moisture from the radiation field.

4. Data for radiative flux calculations

a. Basic sounding data

The basic data used for this study were the averaged soundings presented in Betts and Albrecht (1987). Six of these were averages of FGGE dropwindsonde data over the equatorial Pacific (between 3°–10°N for two regions, 125°–155°W and 160°W–175°E), representing the thermodynamic structure of the undisturbed CBL when a low-level inversion or stable layer was present. Each was the average of some 10–20 dropsondes within these areas during the months (Jan–Feb 1979) of the first FGGE Special Observing Period (SOP-1). We shall take these averages as representative of time scales of order several days and an area of order $(1000\ \text{km})^2$. Although detailed cloud fraction information is not available, the typical cloud cover is scattered trade cumulus. We took the average soundings as representative of the undisturbed environment and used them for the clear air radiative flux computation. The sounding data was only available between the surface and 600 mb, so we interpolated between the 600 mb data and the mean tropical atmosphere at 200 mb and used a mean tropical sounding above 200 mb.

The radiative computation for the cloudy CBL (see section 5) assumed idealized plane parallel clouds, and used cloud thermodynamic parameters which were derived from the clear air sounding (the FGGE data) using a mixing line model (Betts, 1985).

b. Mixing line model for cloud parameters

Each of the average soundings had a distinct mixing line structure (Betts, 1982a) within the CBL, and the CBL top was well defined by a θ_e minimum (Betts and Albrecht, 1987). We generated a "cloud region" temperature and liquid water profile using a mixing line model. Figure 2 illustrates the construction using one of the FGGE profiles (FG141: see Table 1). A mixing line (heavy dashes) was constructed between the saturation points of air at the CBL top ($\mathbf{T}_1$) and air at 1008 mb near the base of the subcloud layer ($\mathbf{M}_0$). A hypothetical cloud region temperature and saturation mixing ratio profile (light solid line) was then recovered from the mixing line following Betts (1982b, 1985) by specifying the gradient of saturation level pressure, $\beta = dp^*/dp$, and integrating from the 1008 mb level. Cloud base (p_B^*) was chosen as the saturation level of the 1008 mb air. For the subcloud layer, we specified $\beta = 0$ (which gives a well-mixed subcloud layer), and from cloud base to one level below the CBL top (we used 10 mb layers within the CBL), we specified $\beta_C = 0.6$. This gives realistic cloud layer gradients of θ and q for these shallow clouds, with an in-cloud liquid water content (LWC) which is at all levels a fixed fraction of the adiabatic liquid water content of $(1 - \beta_C) = 0.4$ (Betts, 1982b). This is an acceptable mean value for small cumulus (Warner, 1970). The cloud LWC increases monotonically to one level below cloud top, and then it is allowed to fall to zero at the next model level (the cloud top). The insert to Fig. 2 shows this LWC profile. This was done to represent the important radiative temperature at the evaporating cloud top boundary where LWC = 0. This temperature is T_{CT} on the mixing line in Fig. 2. The radiation code, discussed in the next section, used the computed LWC and cloud temperature profile as well as the temperature at the evaporating cloud top.

The distribution of cloud top height is of great importance radiatively. Observational studies have shown that cloud tops are often lognormally distributed, but in view of the other assumptions inherent in the radiative model, such as plane parallel clouds, the simple assumption was made that there was a uniform distribution of cloud top heights from two levels above cloud base to one level below the CBL top. Typically this meant 10–15 classes of cloud. For each, the in-cloud thermodynamic profiles (light solid lines in Fig. 2) were used up to one level below cloud top and a cloud top temperature was computed for LWC = 0 at the cloud top pressure. The light dashed lines show the T and LWC profiles for a lower cloud top. We chose for simplicity not to compute a separate mixing line for each cloud top, since the clear air soundings themselves lie close to a mixing line (Betts and Albrecht, 1987), and we have made a large simplification in assuming one constant value of β_C and a uniform distribution of cloud top heights within the cloudy CBL. We used the clear air thermodynamic profiles above each cloud top.

5. CBL radiative flux computation

a. Basic procedure

We have estimated radiative fluxes through and above the CBL using the radiation model discussed below. One-dimensional radiative flux computations were made for the clear (unsaturated) atmospheric profile, using derived cloudy thermodynamic profiles (see 4b) for each cloud class, assuming "plane-parallel" clouds. Radiative fluxes were then averaged for different

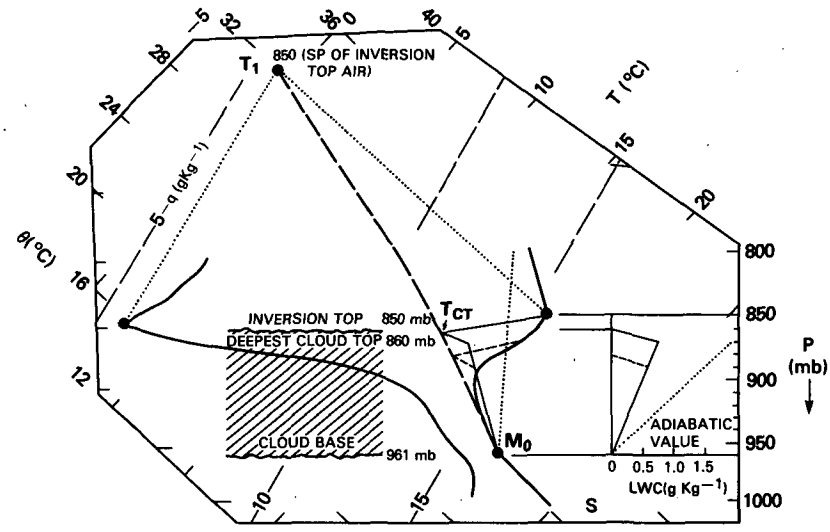

FIG. 2. Tephigram showing CBL thermodynamic structure. The clear air temperature and moisture profiles within the CBL are shown as heavy solid lines. The mixing line between the base of the subcloud layer, M_0, and the CBL top air, T_1, is shown as heavy dashes. The cloud region temperature profile for the deepest cloud class is shown as a light solid line. This lies between the moist adiabat (dotted) and the mixing line in the ratio 0.6/0.4 as shown, corresponding to $\beta_c = 0.6$ (see text), up to one level below cloud top, where cloud-top temperature is T_{CT} on the mixing line and LWC = 0. Insert on right shows the corresponding profile of LWC, which is 40% of the adiabatic value. The short dashed lines are the profiles for a lower cloud top. One pair of dotted lines shows the construction of T_1 from the temperature and dewpoint of inversion top air. S marks the ocean surface temperature and pressure.

specified total cloud fractions (0–50%). The total cloud fraction was distributed uniformly among the number of classes of clouds, each with a different cloud top, as discussed above.

b. *Radiation model*

Radiative heating and cooling rates were calculated using a one-dimensional radiative flux model based on that used in the UCLA/GLA GCM (Harshvardhan et al., 1987). The model includes longwave and solar components, and can be used for clear sky or partially cloudy conditions. We computed fluxes and heating and cooling rates every 10 mb within the CBL. The longwave model accounts for absorption and emission by water vapor, carbon dioxide, and ozone, and treats clouds as multilayer absorbers that are nearly black, but with single-layer emissivities based on cloud liquid water. The shortwave model includes absorption by water vapor, absorption by ozone above any cloud layer, nonconservative multiple scattering by cloud droplets, and direct and diffuse reflection by the ocean surface.

The radiative model requires that a few parameters and the important vertical atmospheric profiles be specified. Surface temperature, surface albedoes for scattering of direct and diffuse solar radiation, and the solar zenith angle are specified. We used a daytime mean solar zenith angle of 54.4° corresponding to 7°N and 1 February. (We found that the error introduced by using one mean solar zenith angle was small.) The key vertical profiles are temperature, humidity, and liquid water concentration for the cloud regions, and separate temperature and humidity structures for clear regions. A climatological carbon dioxide concentration and a reference ozone mixing-ratio profile are used. The temperature and moisture profiles are taken directly from the atmospheric data in clear air, or derived from the mixing line model within cloud (see section 4b).

Our primary extension of Harshvardhan et al. (1987) was to treat cloudiness consistently in the solar and longwave computations by using a common liquid water profile derived from the mixing line model dis-

TABLE 1. Estimation of ω_T (30% cloud cover).

Dataset	p_{T_1} (mb)	$\overline{\partial\theta/\partial p}$ [K (100 mb)$^{-1}$]	$\bar{\theta}_N$ (K day^{-1})	ω_T (mb day^{-1})
FG112	810	4.66	1.88	40.4
FG113	770	4.90	1.87	38.1
FG114	730	4.89	1.67	34.2
Subset mean		4.82	1.81	37.5
FG141	850	3.52	1.20	34.0
FG142	810	4.72	1.50	31.7
FG143	780	3.74	1.46	39.1
Subset mean		3.99	1.39	34.9
Mean of set		4.40	1.60	36.2

cussed in section 4b. Both the longwave and solar fluxes are sensitive to cloud fraction, cloud thickness, cloud top and cloud base heights, and droplet size distributions. Since microphysical information can only be inferred using the meteorological datasets under study, a few simple climatological relationships are used to obtain cloud infrared and shortwave optical properties from the vertical liquid water profile. For instance, following Fouquart (1985), the effective dropsize (R_E) is assumed to vary linearly with the local liquid water density according to the empirical relationship

$$R_E \approx 11\text{LWC} + 4 \tag{24}$$

where liquid water concentration (LWC) is given in g m^{-3}, and effective radius (R_E) is given in microns. Shortwave single-layer optical thickness is inferred from the layer dropsize and column water amount according to (Stephens, 1978)

$$\tau = 3\text{LWP}/2R_E \tag{25}$$

where liquid water path (LWP) is in g m^{-2}. The longwave cloud layer emissivity is given in terms of these parameters by (Stephens, 1978):

$$\epsilon = 1 - \exp(-0.15\text{LWP}). \tag{26}$$

With these assumptions, the cloud radiative properties can be derived from the liquid water, vapor, and temperature profiles.

The longwave radiation model relies on parameterizations of gas-diffuse transmittance functions, appropriately weighted by Planck blackbody source terms, which span the expected range of temperatures. Included are water vapor line and continuum absorption, carbon dioxide absorption through band centers and band wing regions, and IR ozone-absorption bands. In each case, gas amounts are obtained by scaling actual amounts to their homogeneous path equivalents at well-chosen reference pressure levels. Water vapor and carbon dioxide band absorptances use a parameterization of precomputed line-by-line results by Chou and Peng (1983) and Chou (1984). Continuum absorption in the water vapor window follows the empirical formula of Roberts et al. (1976), while ozone band absorptance is taken from Rodgers (1968). Clouds are treated as stacked semi-opaque layers with broadband emissivities determined from liquid water content according to (26). These emissivities are typically quite close to unity for modest cloud thicknesses.

Solar radiation is absorbed by water vapor and ozone, scattered by cloud droplets, and reflected at the surface. Near-infrared water vapor bands are treated using a five-term exponential-sum infrared transmission function following Lacis and Hansen (1974); the ozone parameterization also uses their absorption formula. Plane-parallel clouds are assumed to provide fractional coverage and are modeled with a delta-Eddington two-stream flux model (Joseph et al., 1976; King and Harshvardhan, 1986). The spectral dependence of the droplet single-scattering albedo is approximated by using two values, 1.0 for visible wavelengths and 0.99 in the near infrared.

Cooling rate profiles near cloud top are quite sensitive to the model IR emissivity assumption, but bulk cooling rates for the cloud and boundary layer are generally not affected by these details. The clear sky component of the longwave model was compared against line-by-line calculations by Harshvardhan et al. (1987) as part of the intercomparison of radiation codes in climate models study (ICRCCM, 1984), and on the basis of these comparisons we expect cooling rates to be accurate to within about 0.2°C day^{-1}. Solar heating rates in the boundary layer are considerably more sensitive to how clouds are modeled. The present model uses a very simple representation of the spectral dependence of liquid water absorption, which might be expected to limit the accuracy of the computed solar heating rates. The two-stream multiple scattering models give reasonable accuracy for thick clouds. However, the treatment of the clouds as plane parallel introduces significant errors (McKee and Cox, 1974), but in this study, where we do not have cloud fraction data, the results will be used simply to show the qualitative dependence on cloud amount.

c. *Example*

Figure 3 illustrates the steps in generating a radiative heating rate profile for a partially cloudy boundary layer. We show four panels, derived from the CBL thermodynamic profiles shown in Fig. 2. Figure 3a is the clear sky longwave (infrared), shortwave (solar) and net heating rates from the surface to 700 mb. Figure 3b shows the corresponding heating rates for a single cloud type: the deepest boundary layer cloud in Fig. 2, with a base at 960 mb and a top at 860 mb, and the liquid water profile shown in Fig. 2 which is 0.4 of the adiabatic value up to 870 mb. There is a large longwave cooling near cloud top and a corresponding substantial shortwave warming, which penetrates more deeply into the cloud. Note that Fig. 3b has a different scale for the heating rate than Figs. 3a, c, and d. Figure 3c shows the corresponding profiles after averaging over all cloud depths, where we assumed a uniform distribution of cloud tops from 860 to 940 mb. This distributes the cloud top radiative cooling through cloud layer. The difference between Figs. 3c and 3a is a measure of the radiative perturbation associated with the cloud fraction: cooling from 860 to 940 mb and warming below from 940 mb to the surface. The final panel, Fig. 3d, is the final average for a 30% cloud fraction: a weighted average of 3a and 3c. It shows a typical profile in which the presence of cloud in the CBL gives enhanced cooling in the upper part of the CBL (860–940 mb) and reduced cooling below, when compared with the clear sky profiles.

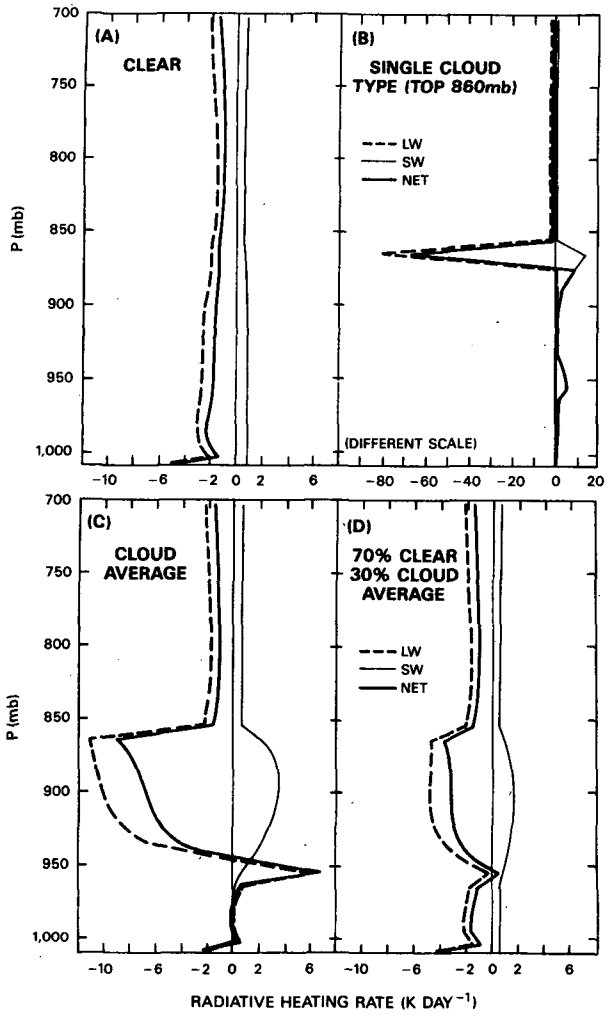

FIG. 3. (a) Computed radiative heating rates for clear sky, (b) single cloud type with top at 860 mb (note different scale), (c) cloud average over all cloud types, and (d) mean for a 30% cloud fraction.

6. Results

The data we used for this analysis were six averaged soundings over the equatorial Pacific from Betts and Albrecht (1987). These soundings show a characteristic mixing line structure up to a θ_e minimum which corresponds closely to the θ_{es} maximum at the inversion top. The soundings were arranged in groups according to CBL top based on this θ_e minimum and θ_{es} maximum. Table 1 shows the datasets and CBL top pressures, p_{T_1}.

a. Estimation of subsidence ω_T

We used the 50 mb layer above cloud top [data levels from $(p_{T_1} - 10)$ to $(p_{T_1} - 50)$] to estimate ω_T using (23). Table 1 shows the average lapse rates, $(\overline{\partial\theta/\partial p})$, radiative cooling rate, $\bar{\theta}_N$, and derived value of ω_T for a 30% cloud fraction. These values were used subsequently. The sensitivity to cloud fraction is very weak. The $\bar{\theta}_N$ and ω_T only increase 2% for an increase of cloud fraction from 0% to 50%.

The $\bar{\theta}_N$ is computed from the radiative model cloud fraction and cloud top distribution, and is subject primarily to any systematic errors in the model formulation. Variability of $\bar{\theta}_N$ is quite large and reflects differences in the thermodynamic structure and CBL depth for the six datasets.

The range of values of ω_T is small (32–40 mb day^{-1}) and may not be significant. These values are comparable to our estimates in section 2 of 32–37 mb day^{-1}. Although our sample of six datasets is too small to draw statistically significant conclusions, the thermal structure, $(\overline{\partial\theta/\partial p})$, and radiative cooling rate, $\bar{\theta}_N$, appear to be weakly correlated, and consequently the derived ω_T is uncorrelated with $\bar{\theta}_N$ and has a smaller percent variability.

This subsidence rate could be systematically underestimated because of the procedure used to generate the six average soundings. The soundings were grouped by CBL top into 40 mb ranges to generate the six averages, so that there has already been some smoothing of the θ_{es} maximum at the CBL top, and the moisture structure. The smoothing of the θ_{es} maximum will increase the magnitude of $\partial\theta/\partial p$ in comparison with a composite of the individual soundings with respect to their θ_{es} maxima at the CBL top. The smoothing of the moisture profile will reduce the radiative cooling rate above the CBL top. Both effects will reduce the computed value of ω_T. However, it could also be argued that individual soundings are not area averages and our six mean profiles *might* be considered representative of a larger space and time average. This remains an uncertainty in this analysis.

b. Sensitivity to shape of divergence profile within the CBL

Another limitation of this analysis is that we estimate the subsidence ω_T just above the CBL top, and then assume a divergence profile within the CBL. The surface fluxes are quite sensitive both to ω_T (section 6c) and (because the CBL is not well mixed) to the shape of this divergence profile. We investigated the sensitivity to three ω profiles within the CBL: these are shown in Fig. 4 for ω_T = 40 mb day^{-1}. Curve 1 has constant divergence, so that ω increases linearly with height. Curve 2 has ω quadratic with height with a local maximum at cloud top, and curve 3 has a local maximum at 0.75 of the CBL depth to simulate the subsidence maximum at the inversion base which has been noted in several CBL budget analyses (Holland and Rasmusson, 1973; Augstein et al., 1973, 1974).

The two components of (21) were used to generate profiles for the convective fluxes of liquid water static energy and total water for the six datasets, which were then averaged. Figure 5 shows the shift of these mean

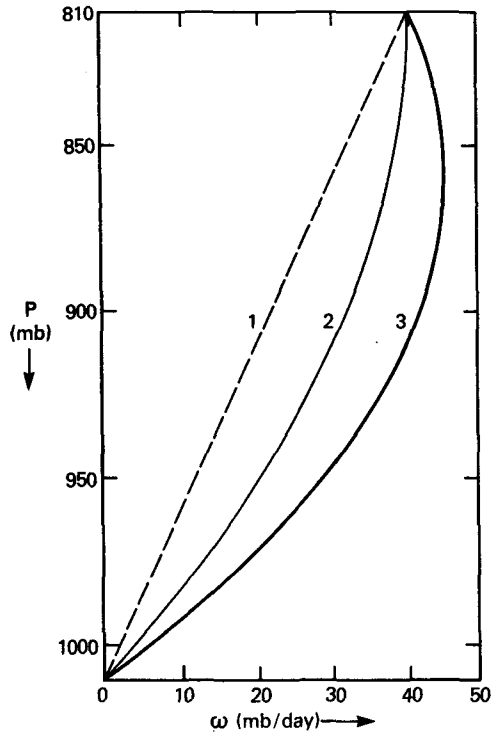

FIG. 4. The three boundary layer ω profiles used for diagnostic computation. Example shown is for ω_T = 40 mb day^{-1}, CBL top at 810 mb. Curve 1 is a linear profile (divergence independent of height), curve 2 is quadratic with ω a maximum at CBL top, and curve 3 is quadratic with a maximum at 0.75 of the CBL depth.

flux profiles with changing divergence profile: the trend from profile 1 to 3 is very similar to the trend with increasing ω_T shown in Fig. 6. Because ω_T may be underestimated by our diagnostic procedure (see 6a), and there is some observational support (loc. cit.) that the subsidence maximum in oceanic CBLs is below the inversion top, we have chosen to use divergence profile 3 in sections 6c, d and e.

c. *Sensitivity to* ω_T

Figure 6 shows the sensitivity of the mean flux profiles to errors in ω_T. The ω_T was set to 35, 40, 45 mb day^{-1} for each dataset and an average of the six flux profiles was computed for a 30% cloud fraction and divergence profile 3 in Fig. 4. As expected, there is a systematic trend with ω_T. Table 2 shows the trend of the surface fluxes with ω_T. For the smaller values of ω_T (comparable to those in Table 1), the surface flux values of $F_{Lq} \approx 130$ W m^{-2} and $F_s \approx 10$ W m^{-2} are comparable to those derived from earlier studies (Augstein, 1978). The F_{Lq} increases with ω_T by 3.5 (W m^{-2})/(mb day^{-1}) and F_s decreases by -1.3 (W m^{-2})/(mb day^{-1}). We see that for ω_T = 45 mb day^{-1}, the surface sensible heat flux has become negative and unrealistic.

d. *Flux estimates using diagnosed* ω_T

Equation (21) was used to generate profiles for the convective fluxes of liquid water static energy and total water for each dataset for cloud fractions of 0–50%, using the values of ω_T diagnosed in section 6a. Table 3 shows the surface fluxes for 0, 30%, and 50% cloud cover. There is considerable variability; the surface latent heat fluxes are in the range 100–150 W m^{-2}, and surface sensible heat fluxes are in the range -5 to $+22$ W m^{-2}. The mean values for the six datasets show a trend with cloud fraction (see section 6e). These mean surface flux values are also comparable to those derived from earlier studies (Augstein, 1978). Figure 7 shows the six pairs of flux profiles for a 30% cloud fraction. The scatter is considerable, but the shape of the flux profiles with height in Fig. 7 is also similar to earlier studies, with F_{sl} going negative in the cloud layer and F_{Lql} falling sharply to zero in the inversion layer (Betts, 1975). The kinks at cloud base are discussed in the next section.

e. *Sensitivity to cloud fraction*

This is a sensitivity study since we have no observations of mean cloud fraction for these average soundings: they were selected based on the presence of low-level inversions in the sounding structure (Betts and Albrecht, 1987). For each cloud fraction (0–50%), the six pairs of flux profiles (each similar to Fig. 7) were averaged to give a mean flux profile. Figure 8 shows the derived fluxes for increasing cloud fraction. Both the radiative fluxes and the mean θ,q structure change with cloud fraction. The increase in the derived total water flux comes entirely from the increase in area

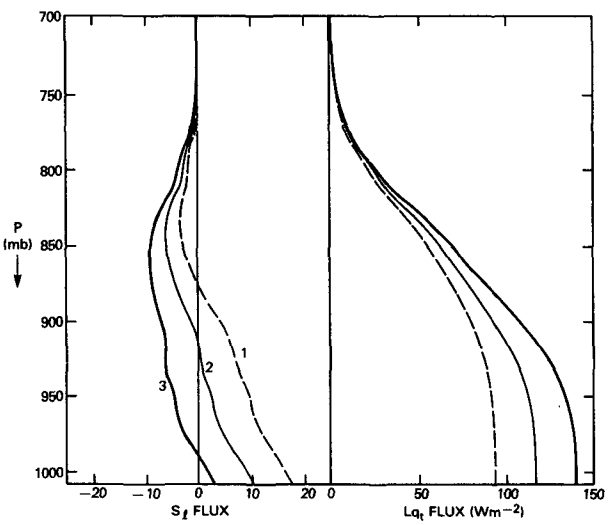

FIG. 5. Dependence of mean convective flux profiles on divergence structure within CBL (for 30% cloud cover and ω_T = 40 mb day^{-1}). Left panel: liquid water static energy (s_l) flux; right panel: the total water flux (note different scales).

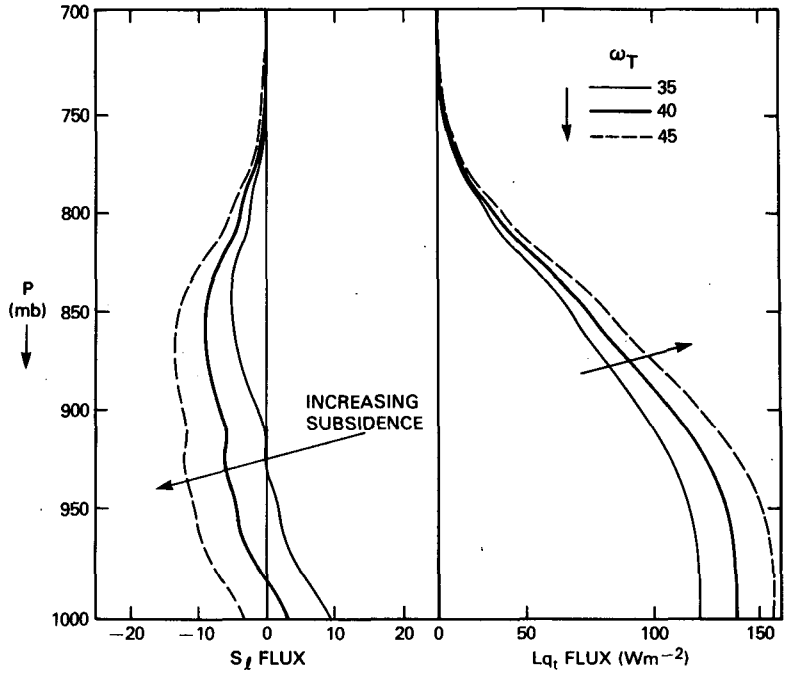

FIG. 6. Dependence of mean convective flux profiles on cloud-top subsidence, ω_T, for divergence profile 3 (Fig. 3), and 30% cloud cover.

total water with increasing cloud fraction, since the very small sensitivity of ω_T to cloud fraction has been ignored (section 6a). However the change in the derived s_l flux is dominated by the radiative flux change associated with increasing cloud fraction. This is because the net cooling of the whole CBL increases with cloud fraction, and within the CBL the net radiative warming at cloud base and cooling at the distributed cloud tops reduce the requirement (in this diagnostic model) for a negative convective s_l flux in the cloud layer. A noticeable kink develops in F_{sl} at cloud base, where the net radiative heating is concentrated. Figure 9, which shows the s_l fluxes for the two datasets' subsets, shows this more clearly. FG112, 113 and 114 had a cloud base near 935 mb, while FG141, 142 and 143 had a lower cloud base near 965 mb. We would expect a negative s_l flux in the cloud layer (Betts, 1973, 1975), associated with the upward advection of liquid water coupled with the maintenance of the cloud field. However, as the cloud fraction increases in Fig. 9, this region of negative s_l flux disappears, so we conclude that the observed thermodynamic structure is compatible only with a small cloud fraction (<30%). Small cloud fractions are typically observed with shallow convective boundary layers over the oceans, so this diagnostic result is reasonable. The heavy solid curve for 30% cloud cover will be regarded as our best diagnostic estimate of the convective fluxes: the surface sensible and latent heat fluxes are 9 and 127 W m^{-2}, respectively (see Table 3).

TABLE 2. Variation of surface fluxes (W m^{-2}) with ω_T (mb day^{-1}) for 30% cloud cover.

	ω_T					
	35		40		45	
Dataset	F_s	F_{Lq}	F_s	F_{Lq}	F_s	F_{Lq}
112	6.6	125.2	0.8	143.1	−5.0	161.0
113	12.4	127.5	5.7	145.8	−0.9	164.0
114	14.7	129.3	6.7	147.7	−1.4	166.2
141	9.6	118.8	5.0	135.8	0.4	152.7
142	14.0	120.0	8.4	137.1	2.8	154.2
143	4.0	113.3	−2.9	129.5	−9.7	145.7
Mean of set	10.2	122.4	4.0	139.8	−2.3	157.3

f. Discussion

We have explored the coupling of the convective and radiative fluxes using a one-dimensional diagnostic model. The uncertainty in the analysis is considerable but nonetheless a consistent picture emerges. Our estimates of the CBL subsidence from the thermodynamic structure and radiation field are of order 35 mb day^{-1}, similar to those suggested by the simplified analysis in section 2. We suspect our values may be a little low because of the averaging procedure. The surface fluxes are quite sensitive to the distribution of divergence within the CBL, so this profile is of considerable interest to future research. The dependence of

TABLE 3. Variation of surface fluxes (W m^{-2}) with cloud cover.

Dataset	ω_T (mb day^{-1})	Cloud cover (%) 0 F_s	0 F_{Lq}	30 F_s	30 F_{Lq}	50 F_s	50 F_{Lq}
FG112	40.4	−3.8	141.5	0.3	144.6	3.0	146.6
FG113	38.1	4.7	134.4	8.3	138.8	10.0	141.8
FG114	34.2	12.6	121.9	16.0	126.3	18.3	129.2
Subset mean				8.2	136.5		
FG141	34.0	4.4	113.1	10.6	115.4	14.6	116.9
FG142	31.7	11.8	105.1	17.7	108.7	21.6	111.0
FG143	39.1	−5.0	122.1	−1.6	126.6	0.6	129.2
Subset mean				8.9	116.9		
Mean of set		4.1	123.0	8.6	126.7	11.4	129.2

the surface fluxes and convective flux structure on the fractional cloudiness is also interesting. The surface fluxes increase with increasing cloud cover. Both fluxes increase about 1 W m^{-2}/10% cloud cover increase, albeit for different reasons. The sensible heat flux increases because of the increased net radiative cooling of the CBL, and the latent heat flux because of the increase in the mean q_t with cloudiness. Within the CBL, the convective s_l flux increases at all levels as the cloud fraction increases, until the downward transport in the cloud layer disappears around a 40% cloud fraction. Essentially the radiative flux perturbation associated with the cloud field becomes large enough to remove the requirement (in this diagnostic model) for a convective transport in the cloud layer.

This result suggests that shallow clouds have an important radiative role in the atmosphere in maintaining the CBL structure. Our diagnostic study, like earlier budget studies (Holland and Rasmusson, 1973; Augstein et al., 1973), shows a requirement for a downward s_l flux or enthalpy transport (associated with cooling above and warming below) to maintain the mean thermal structure of the CBL. Betts (1973, 1975) attributed this to a convective s_l flux associated with the condensation, upward advection and evaporation of liquid water by the shallow cloud field. However, the radiative perturbation associated with the shallow cloud field, the difference between Figs. 3a and 3c, has qualitatively the same structure: cooling in the upper part of the CBL, and warming below. Our interpretation of Fig.

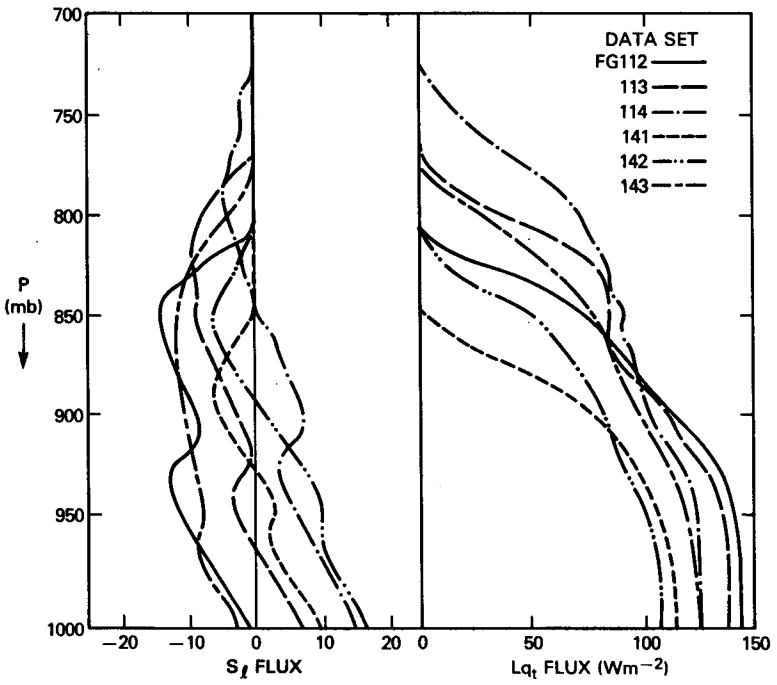

FIG. 7. The s_l and q_t flux profiles for six soundings for 30% cloud cover.

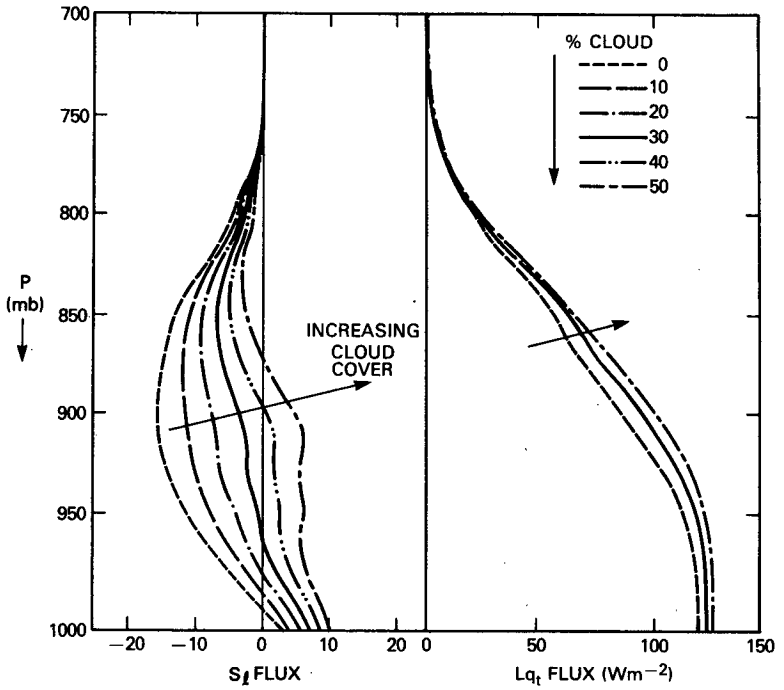

FIG. 8. Mean convective flux profiles for different percent cloud cover.

8 is that as the cloud fraction increases, the corresponding radiative perturbation carries an increasing fraction of the downward heat transport needed to maintain the observed CBL thermal structure (against the subsidence field), until the convective s_l transport in the cloud layer disappears around a 40% cloud fraction. Since we must first have the convective transports to generate the cloud field, we conclude that the ob-

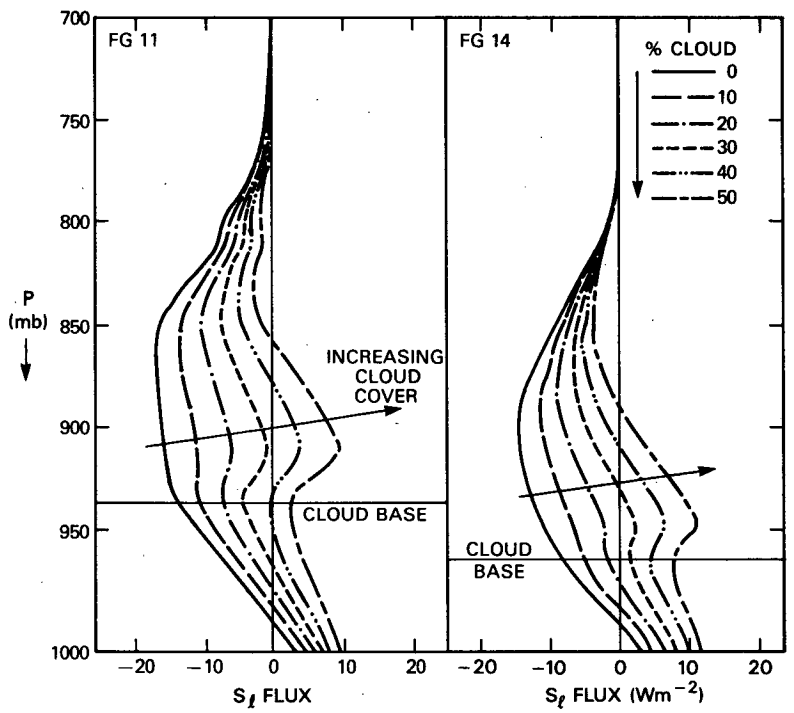

FIG. 9. Mean s_l fluxes for different percent cloud cover for 2 data subsets (FG112, 113, 114 and FG141, 142 and 143) with different cloud bases.

served CBL thermodynamic profiles are consistent with only a small cloud fraction, giving some confidence that the diagnostic results are essentially correct. However, it is also clear that the relative importance of the convective and radiative fluxes associated with shallow cloud fields deserves further study. They both have a similar structure, and both appear to be significant.

7. Conclusions

In the first part of this paper, we presented an idealized energy-balance model for a closed tropical circulation with a well-mixed convective boundary layer (CBL), and showed that the net tropospheric radiative cooling is coupled to a mean subsidence of approximately 35 mb day^{-1} ($\approx$0.04 Pa s^{-1}). This mean subsidence brings drier air down into the CBL. This couples the subsidence and the surface winds to a surface latent heat flux, which we estimated as $\approx$160 W m^{-2}. The moist CBL air, in turn, flows into the tropical convergence zones, where most of the water vapor is precipitated to release the latent heat, which creates the heating gradients, which drive the circulations that balance the radiative cooling. The sensitivity of the surface latent heat flux to processes which affect the net tropospheric cooling is apparent. For example, upper-level clouds, such as thin cirrus which reduce the net tropospheric cooling, will reduce the subsidence and the mean surface latent heat flux. Clearly, this coupling between cloudiness, the tropospheric radiation field and the surface moisture flux will impact the model climate in global simulations.

We then combined a radiation model, which included boundary layer clouds, with a one-dimensional diagnostic model to explore the coupling of the radiation field, the diagnosed mean subsidence, and the boundary layer and surface fluxes for a specific region using mean FGGE sounding data from the equatorial Pacific (from Betts and Albrecht, 1987). We found that the mean subsidence at the top of the CBL was in the range 32–40 mb day^{-1} ($\approx$0.04 Pa s^{-1}) and was largely independent of boundary layer cloud fraction. We found that the diagnosed convective heat flux profiles within the CBL and the surface fluxes were sensitive both to the cloud fraction and the mass divergence profile within the CBL for which we had no direct data. However, if we assumed a divergence profile with a subsidence maximum near the inversion base, consistent with earlier budget studies (Augstein et al., 1973; Holland and Rasmusson, 1973), and a small cloud fraction ($\approx$30%), consistent with scattered trade cumuli, we obtained reasonable surface fluxes of sensible heat $\approx$10 W m^{-2} and latent heat $\approx$130 W m^{-2}. We used radiation fields averaged over 24 hours, but clearly the large difference between day and nighttime cooling rates may modulate the subsidence rate. Gray (1973) and McBride and Gray (1979) have shown a large diurnal variation of the convectively driven mass circulation in the tropics, phase lagged from the time of maximum cooling (midnight) by about 6 hours. The CBL response time to changes in the external forcing is of order days (Schubert et al., 1979), so our analysis which averages through diurnal cycle is probably useful, but clearly the diurnal response of the CBL needs further study.

Within the CBL we studied the effect of changing a specified fractional cloudiness and found that the convective fluxes increased with increasing cloud fraction. Indeed, the radiative flux perturbations associated with a shallow cloud field appeared to be as important as the convective fluxes. We concluded that the observed thermodynamic profiles and (diagnosed) fluxes appear to be consistent with only a small cloud fraction (<30%). The processes controlling fractional cloudiness are not addressed, but they are clearly of great importance to the energy balance of the CBL. There are indeed many questions that this diagnostic analysis cannot address, particularly the controls on boundary layer depth which depend on the complex coupling of the moisture structure, cloudiness and radiative cooling which feeds back on the thermal and virtual potential temperature budget. We hope to address these in another paper using an idealized predictive model. Nonetheless, even the simple diagnostic analyses given here show the importance of the coupling between the surface fluxes, subsidence and the radiation field in the tropics.

Acknowledgments. This work was supported by NASA Goddard Space Flight Center under Contract NAS5-28800, and the National Science Foundation under Grants ATM 84-03333 and ATM 87-05403. We are grateful for helpful discussions with Bruce Albrecht, Joanne Simpson, and Harshvardhan, and for suggestions by the reviewers.

APPENDIX

Relationship of Potential Temperature and Static Energy Budgets

Consider changes in the equivalent potential temperature

$$c_p\delta\theta_e/\theta_e = c_p\delta T/T - R\delta p/p + L\delta q/T. \quad \text{(A1)}$$

Using the hydrostatic relationship

$$\delta p = -\rho g\delta z \quad \text{(A2)}$$

we obtain

$$c_p(T/\theta_e)\delta\theta_e = c_p\delta T + g\delta z + L\delta q = \delta h \quad \text{(A3)}$$

so that changes of moist static energy ($h = c_pT + gz + Lq$) are related to changes in θ_e in a hydrostatic atmosphere. Furthermore

$$c_pF_{\theta_e} = c_p\overline{\omega'\theta_e'} = (\overline{\theta_e/T})\overline{\omega'h'} = (\overline{\theta_e/T})F_h \quad \text{(A4)}$$

if we neglect any correlation of (θ_e/T) with ω'. Hence (4c) is just $c_p(\overline{T/\theta_e})$ times (4b).

Similarly for the liquid water static energy $s_l = c_pT$

$+ gz - L_l$ and liquid water potential temperature θ_l (Betts, 1973, 1975),

$$\delta s_l = c_p(\overline{T/\theta_l})\delta\theta_l. \quad \text{(A5)}$$

We use the θ_l structure in section 6 to compute the s_l budget.

REFERENCES

Albrecht, B. A., A. K. Betts, W. Schubert and S. K. Cox, 1979: A model of the thermodynamic structure of the trade-wind boundary layer. Part I: Theoretical formulation and sensitivity tests. *J. Atmos. Sci.*, **35**, 73–89.

——, V. Ramanathan and B. A. Boville, 1986: The effects of cumulus moisture transports on the simulation of climate with a general circulation model. *J. Atmos. Sci.*, **43**, 2443–2462.

Augstein, E., 1978: The atmospheric boundary layer over the tropical oceans. *Meteorology over the Tropical Oceans*, D. B. Shaw, Ed., Royal Meteor. Soc. 1978, 73–104.

——, H. Riehl, F. Ostapoff and V. Wagner, 1973: Mass and energy transports in an undisturbed Atlantic trade wind flow. *Mon. Wea. Rev.*, **101**, 101–111.

——, H. Schmidt and F. Ostapoff, 1974: The vertical structure of the atmospheric planetary boundary layer in undisturbed trade winds over the Atlantic Ocean. *Bound.-Layer Meteor.*, **6**, 129–150.

Betts, A. K., 1973: Nonprecipitating cumulus convection and its parameterization. *Quart. J. Roy. Meteor. Soc.*, **99**, 178–196.

——, 1974: Further comments on "A comparison of the equivalent potential temperature and the static energy". *J. Atmos. Sci.*, **31**, 1713–1715.

——, 1975: Parametric interpretation of trade-wind cumulus budget studies. *J. Atmos. Sci.*, **32**, 1934–1945.

——, 1982a: Saturation point analysis of moist convective overturning. *J. Atmos. Sci.*, **39**, 1484–1505.

——, 1982b: Cloud thermodynamic models in saturation point coordinates. *J. Atmos. Sci.*, **39**, 2182–2191.

——, 1983: Thermodynamics of mixed stratocumulus layers: Saturation point budgets. *J. Atmos. Sci.*, **40**, 2655–2670.

——, 1985: Mixing line analysis of clouds and cloudy boundary layers. *J. Atmos. Sci.*, **42**, 2751–2763.

——, and B. A. Albrecht, 1987: Conserved variable analysis of the convective boundary layer structure over the tropical oceans. *J. Atmos. Sci.*, **44**, 83–99.

Charney, J. G., 1975: Dynamics of deserts and drought in the Sahel. *Quart. J. Roy. Meteor. Soc.*, **101**, 193–202.

Chou, M. D., 1984: Broadband water vapor transmission functions for atmospheric IR flux computations. *J. Atmos. Sci.*, **41**, 1775–1778.

——, and L. Peng, 1983: A parameterization of the absorption in the 15 μm CO_2 spectral region with application to climate sensitivity studies. *J. Atmos. Sci.*, **40**, 2183–2192.

Fouquart, Y., 1985: Radiation in boundary layer clouds. Rep. of the *JSC/CAS Workshop on Modeling of Cloud Topped Boundary Layer*, Fort Collins, Appendix D. [Available from Dept. of Atmos. Science, Colorado State University, Fort Collins, CO, 80523.]

Gray, W. M., 1973: Cumulus, convection and larger scale circulations. Part I: Broadscale and mesoscale considerations. *Mon. Wea. Rev.*, **101**, 839–855.

Harshvardhan, R. Davies, D. A. Randall and T. G. Corsetti, 1987: A fast radiation parameterization for atmospheric circulation models. *J. Geophys. Res.*, **92**, 1009–1016.

Heckley, W. A., 1985: Systematic errors in the ECMWF operational forecasting model in tropical regions. *Quart J. Roy. Meteor. Soc.*, **111**, 709–738.

——, 1986: Performance of the ECMWF forecasting model in tropical prediction. *Conf. Sci. Results of the First GARP Global Experiment*, Miami, Amer. Meteor. Soc. 75–77.

Holland, J. Z., and E. Rasmusson, 1973: Measurements of the atmospheric mass energy and momentum budgets over a 500 kilometer square of tropical ocean. *Mon. Wea. Rev.*, **101**, 44–55.

ICRCCM, 1984: The intercomparison of radiation codes in climate models (ICRCCM), WCP-93, 37 pp. [Available from World Meteorological Organization, Geneva, Switzerland.]

Joseph, J. H., W. J. Wiscombe and J. A. Weinman, 1976: The delta-Eddington approximation for radiative flux transfer. *J. Atmos. Sci.*, **33**, 2452–2459.

King, M. D., and Harshvardhan, 1986: Comparative accuracy of selected multiple scattering approximations. *J. Atmos. Sci.*, **43**, 784–801.

Lacis, A. A., and J. E. Hansen, 1974: A parameterization for the absorption of solar radiation in the earth's atmosphere. *J. Atmos. Sci.*, **31**, 118–133.

Lilly, D. K., 1968: Models of cloud-topped mixed layers under a strong inversion. *Quart J. Roy. Meteor. Soc.*, **94**, 292–309.

Lorenz, E. N., 1967: The nature and theory of the general circulation of the atmosphere. 161 pp. [Available from World Meteorological Organization, Geneva, Switzerland.]

McBride, J. L., and W. M. Gray, 1980: Mass divergence in tropical weather systems. Paper I: Diurnal variation. *Quart. J. Roy. Meteor. Soc.*, **106**, 501–506.

McKee, T. B., and S. K. Cox, 1974: Scattering of visible radiation by finite clouds. *J. Atmos. Sci.*, **31**, 1885–1892.

Oort, A. H., and E. M. Rasmusson, 1971: Atmospheric circulation statistics. NOAA Prof. Paper No. 5. [Available from U.S. Govt. Printing Office, Washington, D.C., 20402, Document No. 0317-0045.]

Riehl, H., and J. S. Malkus, 1958: On the heat balance of the equatorial trough zone. *Geophys.*, **6**(3), 503–538.

——, and J. Simpson, 1979: The heat balance of the equatorial trough zone: Revisited. *Contrib. Atmos. Phys.*, **52**, 287–305.

——, T. C. Yeh, J. S. Malkus and N. E. LaSeur, 1951: The northeast trade of the Pacific Ocean. *Quart. J. Roy. Meteor. Soc.*, **77**, 598–626.

Roberts, R. E., J. E. A. Selby and L. M. Biberman, 1976: Infrared continuum absorption by atmospheric water vapor in the 8–12 μm window. *Appl. Opt.*, **15**, 2085–2090.

Rodgers, C. D., 1968: Some extensions and applications of the new random model for molecular band transmission. *Quart J. Roy. Meteor. Soc.*, **94**, 99–102.

Sarachik, E. S., 1978: Tropical sea surface temperature: An interactive one-dimensional atmosphere ocean model. *Dyn. Atmos. Oceans*, **2**, 455–469.

Schubert, W. H., 1976: Experiments with Lilly's cloud-topped mixed layer model. *J. Atmos. Sci.*, **33**, 436–446.

——, J. S. Wakefield, E. J. Steiner and S. K. Cox, 1979: Marine stratocumulus convection. Part I: Governing equations and horizontally homogeneous solutions. *J. Atmos. Sci.*, **36**, 1286–1307.

Stephens, G. L., 1978: Radiation profiles in extended water clouds. Part II: Parameterization schemes. *J. Atmos. Sci.*, **35**, 2123–2132.

Warner, 1970: On steady-state one-dimensional models of cumulus convection. *J. Atmos. Sci.*, **27**, 1035–1040.